Journal of Zhejiang University-SCIENCE A (Applied Physics & Engineering)
ISSN 1673-565X (Print); ISSN 1862-1775 (Online)
www.zju.edu.cn/jzus; www.springerlink.com
E-mail: jzus@zju.edu.cn

A new approach to simulate the supporting arch in a tunnel based on improvement of the beam element in FLAC^{3D*}

Wei-teng LI[1], Ning YANG[1,2], Ting-chun LI[†‡1], Yu-hua ZHANG[1], Gang WANG[1]
(*[1]Shandong Provincial Key Laboratory of Civil Engineering Disaster Prevention,*
Shandong University of Science and Technology, Qingdao 266590, China)
(*[2]Jiangsu Vocational Institute of Architectural Technology, Xuzhou 221116, China*)
[†]E-mail: tchli_sd@163.com

Received July 15, 2016; Revision accepted Jan. 21, 2017; Crosschecked Feb. 7, 2017

Abstract: The beam element in FLAC^{3D} can be used to simulate the supporting arch in a tunnel. However, this approach has the shortcoming of its constitutive model, and the bearing capacity and surrounding rock supporting effect of the arch model will be significantly exaggerated. To simulate the supporting arch in tunnel engineering well, a new approach is proposed by improving the beam element. The yield criterion of the beam element subjected to compression-bending loads is established based on the now-available bearing capacity formulas of some typical compression-bending sections. In addition, the yield criterion is embedded in the FLAC^{3D} main program by using the FISH language, and the modification of the beam model and the yielding failure simulation of the supporting arch are finally implemented. Compression-bending tests and roadway tunnel arch support example analysis were performed. The results are as follows: (1) the modified model showed the dependence of the bending moment and axial force on the yielding action of the beam element under compression-bending loads; (2) the implementation program is effective and sensitive; (3) the computing deviation caused by the shortcomings of the original beam element model was effectively suppressed, the mechanical behavior and surrounding rock supporting laws exhibited by the arch model were much closer to reality, and the calculation accuracy and design reliability were improved by the new simulation approach.

Key words: Tunnel; Supporting arch; FLAC^{3D}; Beam element; Yield criterion; Modified model
http://dx.doi.org/10.1631/jzus.A1600508 **CLC number:** TH161.12

1 Introduction

With the rapid increase of mining depths, the development of infrastructure construction, and the increasing numbers of tunnel engineering projects, such as mining roadways, traffic tunnels, subways, and water conveyance tunnels located in complex conditions, tunnel support problems are becoming much more serious. With the increasing difficulties of support in the aforementioned tunnels, the use of arch supports, such as I section steel (I-steel) style, lattice steel girder style, TH section steel (U-steel) style (Brady and Brown, 2004; Wong *et al.*, 2013), and concrete filled steel tube (CFST) style (Chang *et al.*, 2014; Wang *et al.*, 2016a; 2016b), is increasingly common. In addition, the number of failure cases related to arch support is increasing (Wang *et al.*, 2000; Jiao *et al.*, 2013; Rodríguez and Díaz-Aguado, 2013). Some typical failure modes, e.g., buckling and large deformation, are shown in Fig. 1. There is thus an urgent need to study the bearing characteristics of

---

[‡] Corresponding author

[*] Project supported by the National Natural Science Foundation of China (No. 51604166), the China Postdoctoral Science Foundation (No. 2016M590645), the Natural Science Foundation of Shandong Province (Nos. BS2015NJ003 and ZR2016JL018), and the Qingdao Postdoctoral Research Project (No. 2016130), China

ORCID: Wei-teng LI, http://orcid.org/0000-0002-3833-8846; Ting-chun LI, http://orcid.org/0000-0002-1275-0517


(a) (b) (c)

Fig. 1 Cases of support failure with arches in tunnels: (a) arch leg buckling on the left sidewall in a tunnel supported by I-steel arches; (b) arch crown buckling in a mining roadway supported by U-steel arches; (c) huge deformation in a mining roadway supported by CFST arches

tunnel support arches and to propose applicable optimization methods for the support parameters.

Numerical simulation is a powerful means to perform the above-described research. FLAC^{3D} (Fast Lagrangian Analysis of Continua) is a widely used software package that focuses on geotechnical engineering numerical calculation problems (Itasca Consulting Group Inc., 2005; Do *et al*., 2014; Liu *et al*., 2016). In FLAC^{3D}, there are several structural elements, such as the beam element, cable element, pile element, liner element, and shell element, that can simulate support structures and are widely used (Schumacher and Kim, 2013; Nemcik *et al*., 2014; Hegde and Sitharam, 2015; Yu *et al*., 2016b). To simulate an arch support, the beam element is usually selected because the arch model established by the beam element has nearly the same structure as the real one; in addition, the parameter input and result output system is easy to use. Because there is a defect in the beam element when the loads reach or exceed the bearing capacity, the mechanical character shown by the model arch deviates markedly from the real one. This deviation significantly decreases the calculation accuracy and precision. The proof of this disadvantage can be observed in the example analysis in Section 4 of this paper.

Fortunately, there is a second-development platform in FLAC^{3D}. The disadvantages of the structure elements and other requirements can be improved or realized through this platform. However, the development activities are mainly concentrated on the aspect of custom material constitutive relations currently (Wu *et al*., 2011; Latha and Garaga, 2012; Li S.C. *et al*., 2013; Pourhosseini and Shabanimashcool, 2014; Fahimifar *et al*., 2015; Li T.C. *et al*., 2015; Wang *et al*., 2016), and less effort has been spent on the structural element models described in the following. A new anchor bolt model under tensile load was rooted in FLAC^{2D} by Nemcik *et al*. (2014). Through different approaches, Qi *et al*. (2004) and Li *et al*. (2016) modified the cable element in FLAC^{2D} and FLAC^{3D}, respectively. Yu *et al*. (2016a) introduced a modified unit cell approach to model the geosynthetic-reinforced and column-supported embankments supported by deep mixed column walls based on FLAC. In this paper, we introduce a new approach to simulate support arch in tunnel based on an improvement of the beam element in FLAC^{3D} using the above-mentioned second-development platform.

2 Constitutive model of the beam element in FLAC^{3D}

2.1 Basic compositions of the beam element and its working principle

According to the user's manual of FLAC^{3D} (Itasca Consulting Group Inc., 2005), each beam element is defined by geometric and material parameters. A single beam element is assumed to be a straight segment of uniform unsymmetrical cross-sectional properties lying between two nodal points. An arbitrarily curved structural beam can be modeled as a curvilinear structure composed of a collection of beam elements. The coordinate system and forces and moments at the ends of a beam element are shown in Fig. 2. The stiffness matrix of the beam finite element includes all six degrees of freedom at each node to represent the axial, shear, and bending action within a beam structure. Although the beam element is a 3D model, the deformation property in 3D space has not been perfectly developed. Thus, the beam elements are suggested to simulate structural beams in which the displacements caused by transverse-shearing deformations and out-of-plane (longitudinal) warping of the cross section can be neglected. Each beam element possesses 10 properties, six are required (Young's modulus, Poisson's ratio, cross-sectional area, second moment with respect to the beam element y-axis, second moment with respect to the beam element z-axis, and polar moment of inertia), and the last four are optional (density, plastic moment capacity, thermal expansion coefficient, and vector $\boldsymbol{Y}$ defining the y-axis). The action between the beam element and surrounding rock zone element is produced by links, which can transmit forces and deformations.

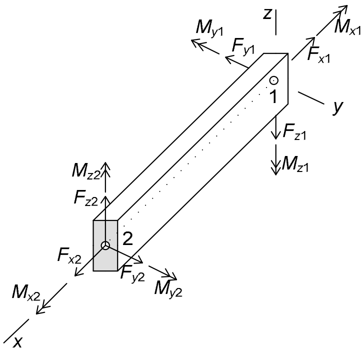

Fig. 2 Coordinate system and sign convention for forces and moments at the ends of a beam element (Itasca Consulting Group Inc., 2005)
M is the bending moment, and F is the axial or shear force

By default, each beam element behaves as an isotropic, linearly elastic material with no failure limit. However, one can specify a limiting plastic moment M_{P} or introduce a plastic-hinge location (across which a discontinuity in rotation may develop) between beam elements; i.e., the section at which the plastic moment occurs can continue to deform without inducing additional resistance after it reaches M_{P}. The plastic-moment capacity limits the internal moment carried by each beam element. From the above analysis, we find that the present formulation in FLAC$^{\mathrm{3D}}$ enables the beam elements to behave elastically until they reach the plastic moment.

2.2 Compression-bending characteristics of the beam element

The inner forces of a supporting arch in underground engineering are always composed of axial forces and bending moments (Section 5.2). Thus, the yielding and failure actions of the supporting arch are determined by the bending ability combined with the compression ability but not by one of them alone. If the supporting arch is to be simulated precisely by using the beam element, it is necessary to study the compression-bending ability of the beam element.

Because it does not consider the out-of-plane deformation, the introduction of the compression-bending property of the beam element and the subsequent model-improvement work is limited to the planar problem. The mechanical model (2D) of the beam element subjected to a compression-bending load is shown in Fig. 3. Under a load composed of an axial force N and a bending moment M, the bending deformation and compressive deformation are determined by the constitutive relations shown in Fig. 4, where k_M and k_M' are the flexural rigidities before and after the bending yielding action, k_N and k_N' are the axial stiffnesses before and after the compressive yielding action, and $\Delta\varphi$ and Δl are the curvature increment and length increment of the model, respectively. The constitutive relation is described below.

2.2.1 Elastic stage

When the loads are low (do not satisfy the yield criterion), the bending and axial deformations are both elastic, the flexural rigidity k_M is EI, and the axial rigidity k_N is EA, where E is the elastic modulus of the beam, and I and A are the moment of inertia and area of the beam cross-section, respectively.

With increasing load, if the plastic moment is not specified, the elastic deformation will continue in the above pattern until the calculation is terminated. This is not in accordance with reality, and the deviation will be more intense when the loads are higher.

2.2.2 Yielding property of the original beam element model

With increasing load, if the plastic moment M_{P} is specified and when the bending moment reaches M_{P}, the yielding action is triggered, and the curves in Fig. 4a become a horizontal line. To distinguish from the modified yield criterion below, this criterion is called the original yield criterion of the beam element model. The yield function can be written as

$$\begin{cases} m=1, \\ n=\infty, \end{cases} \tag{1}$$

where m is the moment coefficient, and n is the axial force coefficient, as shown as

$$\begin{cases} m = \left|\dfrac{M}{M_{\mathrm{u}}}\right|, \\ n = \dfrac{N}{N_{\mathrm{u}}}, \end{cases} \tag{2}$$

where M_{u} is the bending bearing capacity of the pure bending beam, and N_{u} is the bearing capacity of the compression column, which can be obtained through tests or relevant calculation formulas (Han and Yang, 2007; SAC, 2014).

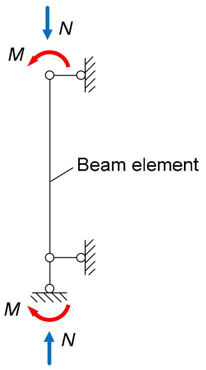

Fig. 3 Mechanical model of the original beam element subjected to compression-bending loads

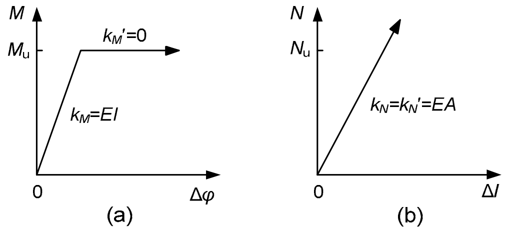

(a) (b)

Fig. 4 Constitutive relations of the original beam element model subjected to compression-bending loads

(a) Bending moment-curvature increment curve; (b) Axial force-length increment curve

Fig. 5 presents the yield criterion diagram determined by Eq. (1), where the horizontal axis is the bending moment coefficient m, and the vertical axis is the axial force coefficient n. The boundary of the shadowed area is the figure representation of the yield function (yield criterion). When the points (m, n), determined by the inner forces, are located in the shadow, the inner forces do not exceed the bearing capacity (point F in Fig. 5). However, when the points are located on the right and top boundary, the sections are just at the yielding critical moment (points G and H in Fig. 5). If the points are located outside the shadow, then the section has already yielded (point J in Fig. 5).

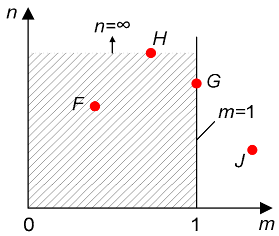

Fig. 5 Yield criterion of the original beam element model subjected to a compression-bending load

The envelope scope of the yield criterion is a half-open infinite interval. From the yield criterion, in the beam element specified plastic moment M_{P}, the yielding of the beam element is found to be only relevant to the bending moment M and is independent of the axial force N. In other words, there is no yielding point in axial deformation, and the axial deformation can develop without limitation. That is clearly not in accordance with reality and thus the original criterion needs improvement.

2.2.3 Post-yield stage

After the trigger action of yielding, the flexural rigidity k_M changes from EI to $k_M'=0$, and the axial rigidity $k_N=EA$ remains unchanged. If the load continues to rise, then the bending moment M will stay at M_{u}, and the axial force N will grow in the elastic mode, regardless of whether it has exceeded the axial bearing capacity N_{u}.

2.2.4 Load path analysis

To clarify the original model, the five main load paths are elaborated with the help of Fig. 6.

1. Load path OA: The bending moment M continues to rise, with the axial force N remaining at zero until m=1. This is in fact a pure bending load path, which corresponds to scheme 13 in Table 1.

2. Load path OBB': This is a typical compression-bending load path. The beam element yields before the axial force N reaches N_{u}, and then, the axial force N continues to grow (and can be infinite) with the

increase in load, while the bending moment M remains at M_u. This load path corresponds to schemes 9–12 in Table 1.

3. Load path OCC': This is another typical compression-bending load path. The beam element yields after the axial force N exceeds N_u, and then the axial force N continues to grow (and can be infinite) with increasing load, while the bending moment M stays at M_u. This load path corresponds to schemes 2–8 in Table 1.

4. Load path OD: The bending moment does not reach the ultimate moment M_u until the end of loading, and the axial force N grows so as to exceed N_u.

5. Load path OE: The axial force N is continuously rising, with the bending moment M staying at zero. This is actually a compression load path and corresponds to scheme 1 in Table 1.

In actual engineering, the yielding property of the component subjected to a compression-bending load should be codetermined by the axial force N and the bending moment M at the least. In the above load paths, determined by the original beam element model, there is just one load path (OA) that exhibits a pure bending load path in conformance with reality. All of the other paths deviate from nature, as the original model has no yielding property in the axial deformation. The above yield criterion and mechanical model do not coincide with the compression-bending property of common components. To elaborate on this disadvantage more clearly, examples were analyzed as detailed in Section 4.

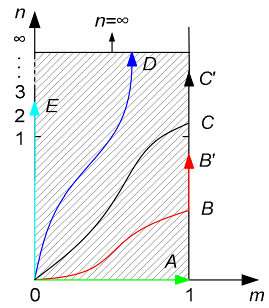

Fig. 6 Diagram of some typical load paths of the original model

3 Improvement of beam element constitutive model and programming implementation

3.1 Modified yield criterion and constitutive model

Because the inner forces of supporting arch sections are mainly axial forces combined with bending moments, the bearing capacity of the supporting arch is always determined by the compression-bending capacity of the cross section. Based on this view, taking the compression-bending bearing capacity formulas as the basis of the yielding judgment, the yield criterion of a beam element subjected to compression-bending loads was established, and the modified criterion formula could then be written as

$$f(m, n) = 1, \qquad (3)$$

Table 1 Test schemes and some results

Scheme No.	Displacement load speed ratio, v_z/v_x	Axial force at the yielding moment (kN)	Bending moment at the yielding moment (kN·m)	Scheme No.	Displacement load speed ratio, v_z/v_x	Axial force at the yielding moment (kN)	Bending moment at the yielding moment (kN·m)
1	0	Infinite	0	A1	0	1084	0
2	0.05	33 450	71.3	A2	0.05	1079	0.14
3	0.1	17 540	71.3	A3	0.1	1070	0.26
4	0.25	6289	71.3	A4	0.25	956.3	11.10
5	0.5	3186	71.3	A5	0.5	857.4	19.65
6	0.75	2184	71.3	A6	0.75	772.8	26.76
7	1.0	1784	71.3	A7	1.0	703.8	32.50
8	1.5	1215	71.3	A8	1.5	595.0	41.37
9	2	779.4	71.3	A9	2	516.7	47.65
10	5	317.0	71.3	A10	5	276.9	64.39
11	10	154.7	71.3	A11	10	149.4	69.28
12	50	29.47	71.3	A12	50	29.35	71.18
13	Infinite	0	71.3	A13	Infinite	0	71.28

where the function expression $f(m, n)$ can be determined using the now-available compression-bending capacity formulas; some of the frequently used sections are listed in Table 2.

A diagram of the modified yield criterion of the beam element subjected to compression-bending loads is presented in Fig. 7. The largest difference between the modified and original criteria is that the axial force N is contained in the constitutive relation of the modified yield criterion in the form of a certain function, and the envelop range is closed. Thus, the yielding of the beam element is determined by bending deformation combined with axial deformation, in contrast to being determined by the bending moment alone as in the original criterion. It is obvious that the modified criterion is more in accord with reality than the original criterion. Moreover, the envelope range area of the modified criterion is much smaller than that of the original criterion; i.e., the original criterion will lead to an exaggeration of the bearing capacity of the beam element subjected to a compression-bending load.

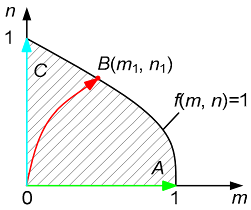

Fig. 7 Modified yield criterion of a beam element subjected to compression-bending loads and some typical load paths

When the modified criterion is used, the constitutive relation of the beam element subjected to compression-bending loads (Fig. 8) is changed accordingly. The modified constitutive relation is detailed below.

3.1.1 Elastic deformation stage

The elastic deformation stage is the same as the original one (Section 2.2).

3.1.2 Yielding property of the modified beam element model

With the increase of loads, when m and n satisfy the criterion Eq. (3) exactly, the beam element is deemed to begin to yield. Taking the load path OB in Fig. 7 as an example, the yielding point is $B(m_1, n_1)$; thus, the yielding forces are $M=m_1M_u$ and $N=n_1N_u$, corresponding to the values of the vertical coordinates of the inflection points on the constitutive relation curves in Fig. 8.

3.1.3 Post-yield stage (yielding response)

The material of a support arch is always steel or a CFST, and thus the constitution relationship can be

Table 2 Compression-bending yield function of some common cross sections

Cross section type and parameter	N_u (kN)	M_u (kN·m)	Yield function $f(m, n)$
I section rib, I-22b	1083.7	71.3	$\begin{cases} m+1.485n^2=1, & n\le 0.4, \\ m+0.126n^2+1.09n-0.217=1, & n>0.4, \end{cases}$
TH section rib (U-steel), U36	1457.6	48.3	Positive bending: $\begin{cases} m+0.717n^2+0.062n=1, & n\le 0.3017, \\ m+0.51n^2+0.685n-0.1951=1, & n>0.3017, \end{cases}$ Negative bending: $\begin{cases} m+1.2525n^2+0.1810n=1, & n\le 0.3122, \\ m+0.479n^2+0.5755n-0.05=1, & n>0.3122, \end{cases}$
CFST with square section; Length of side 150 mm, thickness 8 mm, concrete grade C40	2526	101.7	$\begin{cases} 1.365051n^2-0.4119624n+m=1, & n<0.30179, \\ n+0.69821m=1, & n\ge 0.30179, \end{cases}$
CFST circular section; Diameter 159 mm, thickness 8 mm, concrete grade C40	2184.6	68.6	$\begin{cases} 2.25798n^2-0.73348n+m=1, & n<0.32484, \\ n+0.67516m=1, & n\ge 0.32484, \end{cases}$

Note: The formulas of I-22b and U36 are derived based on the mechanics of materials (You, 2000); the formulas of the CFST are derived from the research results of Han and Yang (2007) and SAC (2014). Positive bending of the U-steel sections indicates that the opening side of a U-steel section is tensile under the bending moment, whereas a negative bending indicates the opposite regarded as perfectly elastic plastic. As a result, when a yielding action of a supporting arch is triggered, the elastic modulus E can be reduced to zero to simulate the yielding response. However, if E is exactly equal to zero, a fatal error will appear in the structure element calculation part of FLAC^{3D}, and the calculation will be terminated. Based on the above situation, the Young's modulus-reduced coefficient λ is introduced, whose value is nearly but not equal to zero. It can be assigned a very small value such as 1×10^{-4} (the differences of results are sufficiently small to be ignored when the value of λ changes from 0.001 to 1×10^{-5}). When a yielding action is triggered, the following are simultaneously applied: E is decreased to λE, the flexural rigidity k_M is reduced to $k_M'=\lambda EI$, and the axial rigidity k_N is reduced to $k_N'=\lambda EA$.

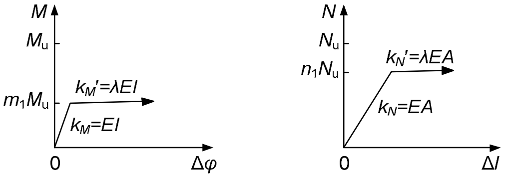

(a) (b)

Fig. 8 Constitutive relations of a modified model of a beam element under compression-bending loads

(a) Bending moment-curvature increment curve; (b) Axial force-length increment curve

Thus, if the loads continue to rise, the bending deformation and axial deformation will continue to develop an elastic constitutive relation; however, the point is that the flexural rigidity is λEI, and the axial rigidity is λEA. This stage corresponds to the lines with a slope of nearly zero in Fig. 8.

3.1.4 Load path analysis

The load paths are described using typical load paths, as shown in Fig. 7.

1. Load path *OA*: This load path is the same as one using the original model and corresponds to scheme A13 in Table 1.

2. Load path *OB*: This is a typical compression-bending load path. When m and n satisfy the modified criterion (see point $B(m_1, n_1)$ in Fig. 7), the beam element yields, and then the deformation will continue while the loads just rise minimally. This load path corresponds to schemes A2–A12 in Table 1.

3. Load path *OC*: This load path corresponds to the load path *OE* in the original model (Fig. 6), with the following difference: when N reaches N_u the load cannot significantly rise. This load path corresponds to scheme A1 in Table 1.

If the point determined by the inner forces M and N is located in the range enveloped by the function curve of $f(m, n)=1$ and the axes, the element is in an elastic status and has not yielded yet. However, when the internal forces satisfy the yield function $f(m, n)=1$ (point B in Fig. 7) the element is determined to act as a yielded member. This model can accurately describe the nature of the deformation and yielding failure of the segment that is subjected to compression-bending loads.

3.2 Implementation program

Fig. 9 shows the technological process of the implementation of the modified model in FLAC^{3D}. In the following statement, the element whose CID (the component-ID number) is j (j=1, 2, …) is taken as an example, where j is the serial number of the beam element. When the model parameters are set (the input of the parameters still obeys the rules of FLAC^{3D}), the calculation is subsequently performed in the main program of FLAC^{3D}.

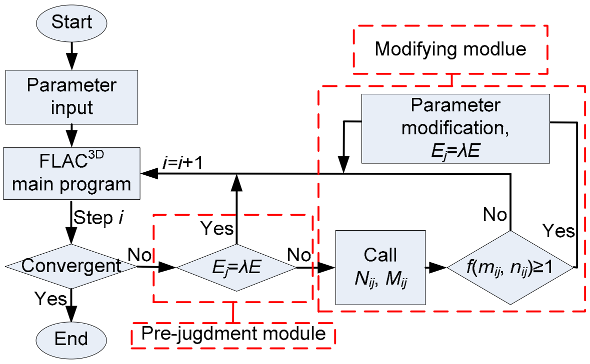

Fig. 9 Implementation process of beam element modification

When the calculation proceeds to step i (i=1, 2, …), the default convergence judgment in FLAC^{3D} is performed, and if the convergence judgment is satisfied, then the calculation is terminated.

If not, then the yielding pre-judgment module is accessed.

1. Pre-judgment module

a. Determine whether Young's modulus E_j is equal to λE; if the answer is yes, then set $i=i+1$ and go to the next step.

b. If not, then the modifying module of the beam element will be entered.

2. Modifying module

a. The axial force N_{ij} and the bending moment M_{ij} of every element are called from the main program, where i is the calculation step, and j is the CID number.

b. The yield criterion is applied. If the yield function $f(m_{ij}, n_{ij})\geq 1$ is satisfied, then verification is conducted, by setting $E_j=\lambda E$ and the other parameters remain unchanged. After these steps, the next calculation step is conducted in the main program using the new parameters.

c. If the inner forces do not agree with the yield function $f(m_{ij}, n_{ij})\geq 1$, then the modifying action is not implemented, and the next step is to continue directly to the main program using the parameters in the last step.

The purpose of the pre-judgment module is to reduce the number of times that the modifying module is called. In this manner, calculation efficiency can be improved and the calculation time be reduced.

The above-described verifying actions are performed using the FISH programming language. Users can obtain the variable values for every calculation step, and the axial force and bending moment of a certain section can be recognized by the two variables as "sb_force" and "sb_mom" (Itasca Consulting Group Inc., 2005). Thus, the N_{ij} and M_{ij} of a certain beam element can be called into the FISH program, and the criterion can be applied. Whether the element has yielded can then be determined. If the criterion is satisfied, then the parameter E will be modified to λE through the variable "sb_emod" (Itasca Consulting Group Inc., 2005). The next step will proceed with the new parameters.

4 Verification of the modified model and implementation program

To address the disadvantages of the original model and verify the modified model and implementation program, numerical examples were conducted in the form of compression-bending tests.

The tested object was an I-steel with section style 22b and length of 1 m. The compression-bending test model is shown in Fig. 10. The total length of 1 m was divided into 20 elements, which were given CID numbers 1 to 20 from left to right; each element length was 0.05 m. The cross-section area was 4.64×10^{-3} m^2, Young's modulus was 2.1×10^{11} Pa, Poisson's ratio was 0.25, the inertia moment I_z was 2.39×10^{-6} m^4, the inertia moment in the bending plane I_y was 3.57×10^{-5} m^4, and the plastic moment M_p was 71.3 kN·m (Table 2). To realize in-plane deformation, all nodes were constrained in the y direction. The node on the left end (node 1) was constrained in all six degrees of freedom to simulate the fixed end. A displacement loading pattern was chosen in the tests, where v_x and v_z are the axial and lateral displacement load speeds, respectively, on the right end. To realize the different loading paths shown in Fig. 6 and Fig. 8, different values of v_z/v_x were set, as shown in Table 1. In addition, the axial load speed v_x was set to a small value of 10^{-5} m/step to simulate the static load. For a comparative study, the original model was used in schemes 1–13, and the new approach was used in schemes A1–A13. In schemes A1–A13, the yield function of I-steel 22b used in the model is presented in Table 2, and the reduced coefficient λ was valued at 1×10^{-4}. The other parameters of both the original approach and the modified approach are the same ones.

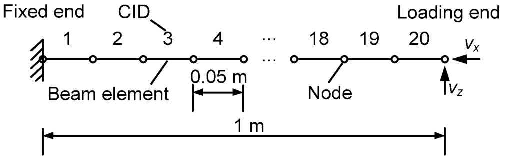

Fig. 10 Numerical model of the compression-bending test

The results of each scheme are listed in Table 1, where the axial force and bending moment were taken from the element that yielded first (this was always the element CID=1 because its bending moment was the largest). Fig. 11 shows the inner force-displacement curves of schemes 7 and A7. To compare and analyze the schemes in a straightforward manner, the axial force and bending moment of some schemes are drawn in the m-n diagram, as shown in Fig. 12.

1. The results of schemes 1–13 in Table 1 show that although the displacement loading ratios were different, the yielding of all of the tested members appeared at the time that the bending moment M

reached 71.3 kN·m. In Fig. 12a, the same law is shown by the phenomenon that all the circle points are located on the same vertical line as $m=1$, with the axial force coefficient n changing by a large margin from 1 to over 30. This result indicates that the yielding of the segments is only relevant to the bending moment M and is independent of the axial force N. Fig. 11a also shows that although the bending moment M reached 71.3 kN·m and yielded, the rising rate of the axial force N did not change at all. Based on the analysis above, we know that bending ability and compression ability are isolated in the original schemes, i.e., that the original model only yields on the bending behavior, and there is no yielding point in the compressive deformation. Thus, there is an obvious deviation between the original model subjected to compression-bending loads and the real segment.

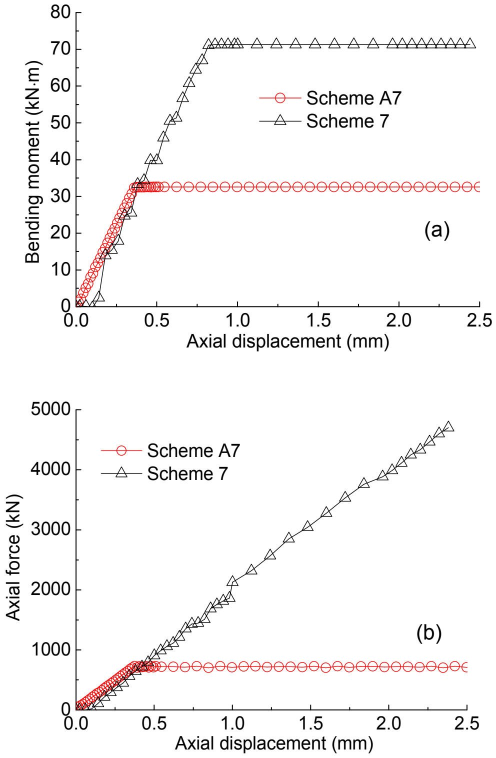

Fig. 11 Inner force-displacement curves of schemes 7 and A7: (a) bending moment-axial displacement curves; (b) axial force-axial displacement curves

2. In Fig. 12b, the inner forces are all located on the m-n curve. The results of the modified schemes are in good agreement with the modified criterion. In other words, the implementation program is effective and sensitive. The dependence of the bending moment and the axial force on the compression-bending member using the modified model was revealed by the calculation results, and the behavior of the modified model was found to be in good agreement with reality.

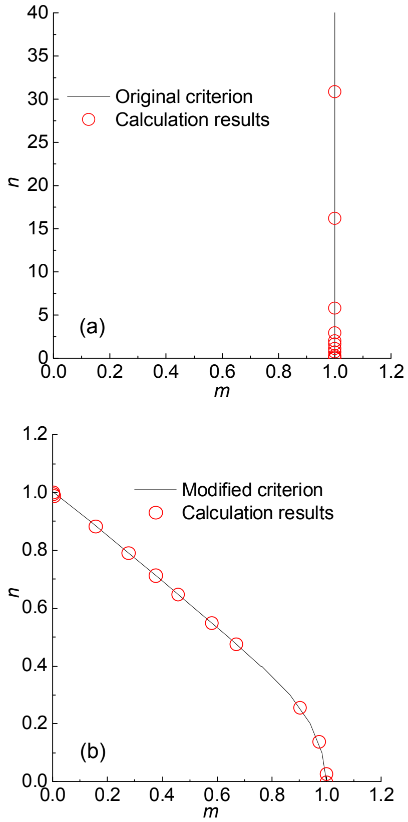

Fig. 12 Inner force figure (*m*-*n*) of the schemes at the yielding moment for the original model schemes (a) and the modified model schemes (b)

3. Comparing the results of the modified model schemes, it is evident that the compression-bending bearing capacity of the original model was obviously exaggerated and was not appropriate for the safety of the design.

5 Verification of the new approach in a roadway tunnel

5.1 Test schemes and parameters

There are eight schemes divided into two groups, as shown in Table 3, and all of the schemes have the same support style and parameters. The first group includes schemes 21–24, and the original model was used in this group. The second group contains schemes A21–A24, in which the new approach was used. In the same group, the ground stress values were different from each other, as shown in Table 3.

The width, height, and thickness of the numerical model were 40 m, 40 m, and 0.8 m, respectively. The shape of the tunnel was semicircular with a straight wall: the radius of the arch was 2.5 m, and the height of the sidewall was 1.5 m. A brick-shaped mesh was used to generate grids, as shown in Fig. 13a. The normal velocities of all nodes on the surfaces except the top were fixed, and the bottom surface was fixed in all directions, whereas the top surface was not fixed; only the compensating ground stress (as shown in the last column of Table 3) was supplied. The ground stress was initialized in all surrounding rock elements, and the values of applied stresses in the three directions (x, y, z) were equal to each other (Table 3). The Mohr-Coulomb model was chosen for the surrounding rock elements; the material parameters are shown in Table 4. The shotcrete liner and supporting arch (I-22b) were installed immediately after excavation. The shotcrete liner was simulated by solid elements, and the thickness was 100 mm (Fig. 13b). The Mohr-Coulomb model was also chosen for use; its material parameters are given in Table 4.

Table 3 Test schemes

Scheme No.	Beam element model	Ground stress value (MPa)	Compensating ground value on the top surface (MPa)
21	Original model	2.5	2.02
22		5	4.52
23		10	9.52
24		15	14.52
A21	Modified model	2.5	2.02
A22		5	4.52
A23		10	9.52
A24		15	14.52

The original beam model and the modified model were each used to simulate the supporting arch. The arch model was arranged at the middle section of the surrounding rock model (Fig. 13b). The supporting arch had a same outline as the shotcrete liner free face, the width was 4.8 m, and the height was 3.9 m. The arch was composed of 56 beam elements, and there were 44 elements in the arch part (CIDs 7–50), and 6 elements in each leg part (CIDs 1–6 or CIDs 51–56). The default properties were adopted in the links between the arch model and the shotcrete liner model. The cross section and mechanical parameters of the arch model including the yield function and

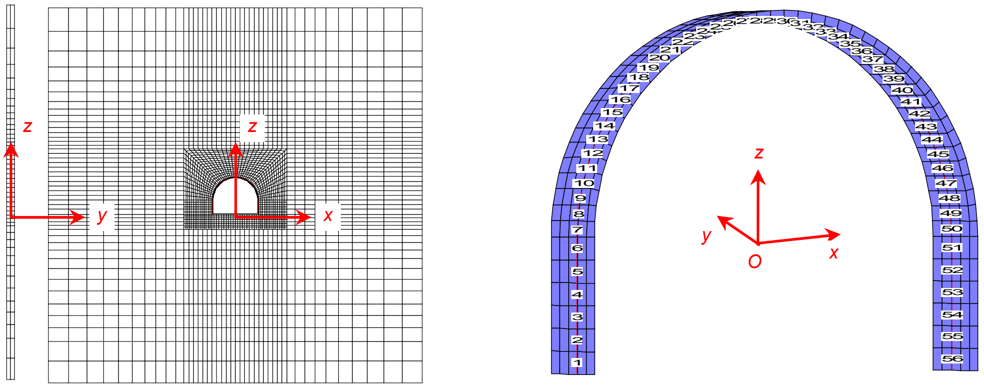

(a) (b)

Fig. 13 Numerical models of surrounding rock (a) and shotcrete liner and supporting arch (b)

Numbers 1–56 are the CIDs of the beam elements

Table 4 Mechanical parameters of the surrounding rock and shotcrete liner

Simulated object	Young's modulus, E (MPa)	Poisson's ratio, μ	Tensile strength, σ_t (MPa)	Cohesion, C (MPa)	Internal friction angle, ψ (°)	Density, D (kg/m^3)
Surrounding rock	2500	0.27	0.8	1.0	28	2400
Shotcrete liner	25 500	0.20	2.0	3.0	50	2400

the Young's modulus-reduced coefficient λ were both the same as those in the example analysis in Section 4.

5.2 Results analyses

The default convergence criterion in FLAC^{3D} was taken as the ending-criterion for the calculation, and the maximum unbalanced force ratio was set to 1×10^{-5}. The results of each scheme are listed in Table 5, where the maximum axial force and maximum bending moment are the maximum values of all elements in the whole calculation process.

5.2.1 Results of the scheme with low ground stress

As shown in Table 5, when the ground stress was 2.5 MPa, all the calculation results (such as the roadway deformations of the modified model schemes) were the same as those of the original model schemes, and the modified influence coefficient (δ) was zero (Fig. 14), because the inner forces of the arch models in schemes 21 and A21 were low and did not reach the modified criterion.

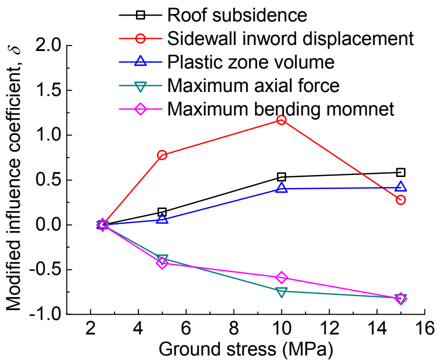

Fig. 14 Curves of modified influence coefficient, δ, with ground stress

$\delta=(R_m-R_o)/R_o$, where R_m is the result of the modified model scheme, and R_o is the original model scheme result

5.2.2 Analysis of the supporting arch mechanical behavior

For schemes 23 and A23, Fig. 15 shows the inner force diagrams of the supporting arch, and Fig. 16 shows the deformation diagrams. Fig. 17 shows the diagram of the inner force of the critical sections at the yielding moment drawing in the *m*-*n* figure, where the scheme serial numbers are labeled near the triangle or circle labels.

1. For the distribution of inner forces on the arch, the inner force diagrams in Fig. 15 conform with the situation in the field: the axial forces are positive and slowly decreasing from top to down; the bending moments cause the inner side of the arch to be pulled on the leg part and develop gradually upward to be compressed before finally being pulled at the crown of the arch. The above-described phenomena indicate that the simulation results agree well with practice and that the inner forces of the arch sections are mainly a combination of the axial force and the bending moment.

2. From the original model scheme results in Table 5, for high ground stress, the axial force N is found to far exceed the axial bearing capacity N_u and to increase further as the ground stress increases. The arch axial force in scheme 24 even exceeded 7000 kN, nearly 7 times the capacity. There is a huge gap between the calculation results and reality in terms of the arch bearing capacity.

3. The inner force diagram of scheme 23 in Fig. 15a shows that the maximum bending moment M at the yielding moment appeared at the middle-upper part of the arch leg; the value was 71.3 kN·m and the axial force was 1213 kN at the same time. In addition, at the end, the axial force N grew obviously and exceeded 4000 kN. In contrast, in scheme A23, the arch

Table 5 Calculation results of each scheme

Scheme No.	Roof subsidence (mm)	Sidewall inward displacement (mm)	Plastic zone volume (m^3)	Maximum axial force (kN)	Maximum bending moment (kN·m)
21	0.87	0.88	15.99	295	7.05
22	5.91	6.57	11.68	1796	19.77
23	18.24	27.67	25.26	4748	71.30
24	37.21	66.13	42.79	7440	71.30
A21	0.87	0.88	15.99	295	7.05
A22	6.74	11.68	12.33	1123	11.34
A23	27.97	60.02	35.42	1237	29.41
A24	58.92	84.51	60.51	1351	12.38

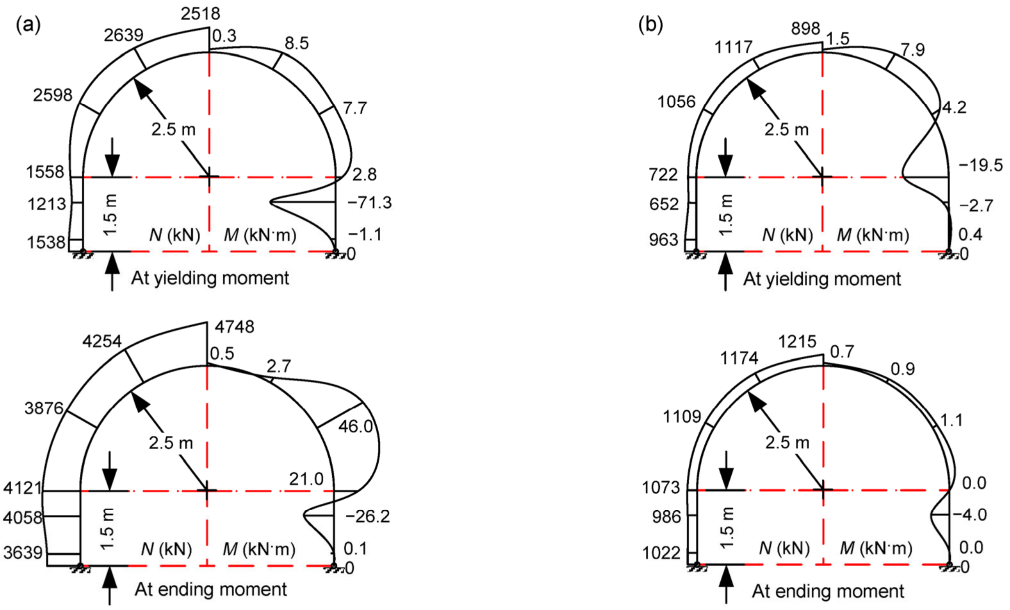

Fig. 15 Inner force diagrams of the supporting arch in scheme 23 (a) and scheme A23 (b)

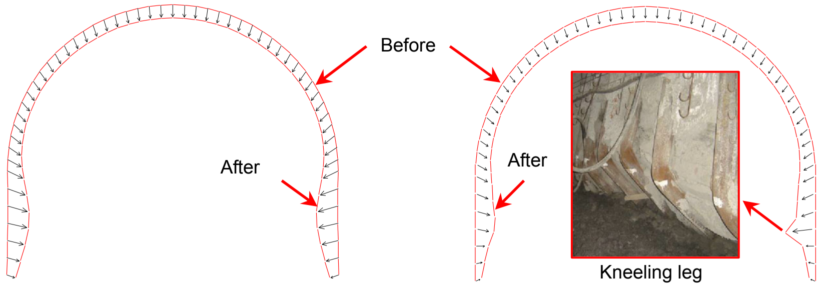

(a) (b)

Fig. 16 Deformation and failure of the arch models in scheme 23 (a) and scheme A23 (b)

model yielded at the moment when the bending moment M reached 19.5 kN·m and the axial force N reached 722 kN at the same time, and the axial force N and bending moment M did not change significantly by the end of the calculation. The values of the inner forces of the modified schemes were remarkably lower than those of the original model schemes (Table 5 and Fig. 15), in good agreement with the actual bearing capacity of the supporting arch.

4. The differences between the results of the modified model schemes and the original model schemes are presented in an m-n diagram as shown in Fig. 17. The smaller the distance between the label and the m-n curve, the higher the calculation accuracy. It is obvious that the deviations in the original model schemes were high and became much higher when the ground stress increased. In addition, the labels of the original model scheme results were all located outside the scope of the envelope; i.e., the capacities of the arch models in the original model

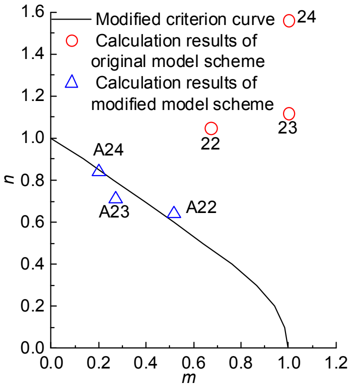

Fig. 17 Inner force figure (m-n) of the critical sections of each scheme at yielding moment

schemes were significantly amplified. For this reason, if the original model is used to design or optimize support, then the parameters will likely correspond to a high risk in real engineering scenarios. Whereas most of the labels of the modified model schemes were located on the *m*-*n* curve. Thus, as a result of using the modified model, the arch model had a more accurate yielding feature, and the implication method was feasible; i.e., the expected objective was reached.

5. In addition, from the calculation results of the modified model schemes in Fig. 17, the inner force labels focused on the upper part of the *m*-*n* curve, the values of n were all greater than 0.6, and the values of m were all less than 0.6; i.e., the axial force made a greater contribution to the yielding of the arch model than did the bending moment in these schemes. Hence, for a semicircular arch with straight legs, the axial force has a remarkable effect on the yielding of the arch and should not be ignored. If the effect of the axial force is not considered in the yield criterion, as in the original beam model, then there may be great deviation in the results.

6. In addition, as shown in Fig. 16b, the right leg of the arch model in scheme A23 presented a buckling failure, in agreement with the "kneeling leg" phenomenon in practice. In addition, an asymmetric characteristic was revealed in the failure of the arch, as shown in Fig. 16b, which we think was caused by the global instability of the arch structure under the pressure of the surrounding rock. The macroscopic bearing characteristic can be simulated more accurately by the modified model than by the original model.

5.2.3 Analysis of the surrounding rock response

Fig. 14 shows the modified influence coefficient curves with the ground stress; the figure indicates the following:

1. The modified influence coefficients of the maximum axial force and maximum bending moment were negative; i.e., the inner forces of the modified model arch were lower than those of the original model. In addition, the modified coefficients of roadway deformation and plastic zone volume were positive. Thus, as a result of the disadvantages of the original model, the original model arch presented a much higher bearing capacity than reality, leading to a significant amplification of the bearing capacity of the supporting arch and the ability to control the surrounding rock deformation and failure.

2. With the increase in ground stress, the absolute values of δ grew; i.e., the difference in the support effect between the original model and the modified model became larger when the ground stress increased.

In summary, the example analysis indicates that because of the disadvantage of the yield criterion of the original beam model, the bearing capacity and support effect were significantly amplified. As a consequence, the design parameters were at a high risk of danger if used in a real engineering project. In contrast, in the schemes using the modified model calculation, the deviations were less, and the mechanical behavior and surrounding rock support effects presented by the arch model were closer to those of field practice; i.e., the calculation accuracy and design reliability were improved.

The proposed new approach is suitable for the simulation of arch support in deep, high-stress, and soft-rock tunnels which have a risk of arch bearing failure. Because the links in FLAC^{3D} still cannot well simulate the interaction of the support arch and the surrounding rock, that shortcoming requires further modification.

6 Conclusions

1. Caused by the defect of the original yield criterion of the beam element, the beam element can yield only on the aspect of bending behavior, and where there is no limit in the axial deformation. The above shortcoming results in significant amplification of the bearing capacity and the surrounding rock supporting effect of the arch model established by the beam elements; the supporting design results are therefore dangerous in an engineering scenario.

2. To improve the beam element, the yield criterion of the beam element subjected to compression-bending loads was proposed based on the now-available bearing capacity formulas of common compression-bending sections, and the modified model was embedded in the FLAC^{3D} main program based on the FISH programming language.

3. Compression-bending tests were performed, and a roadway tunnel arch supporting example was

analyzed. The results show the following: (1) the modified model showed the dependence of the bending moment and axial force on the yielding action of the beam element under compression-bending loads; (2) the implementation program is effective and sensitive; (3) the computing deviation caused by the shortcoming of the original beam element model was effectively suppressed, the mechanical behavior and surrounding rock supporting laws exhibited by the supporting arch using the modified model were much closer to reality, and the calculation accuracy and design reliability were improved.

References

Brady, B.H.G., Brown, E.T., 2004. Rock Mechanics for Underground Mining, 3rd Edition. Kluwer Academic Publishers, Dordrecht/Boston/London.

Chang, X., Luo, X., Zhu, C.X., *et al*., 2014. Analysis of circular concrete-filled steel tube (CFT) support in high ground stress conditions. *Tunnelling and Underground Space Technology*, **43**:41-48. http://dx.doi.org/10.1016/j.tust.2014.04.002

Do, N.A., Dias, D., Oreste, P., 2014. Three-dimensional numerical simulation of mechanized twin stacked tunnels in soft ground. *Journal of Zhejiang University-SCIENCE A (Applied Physics & Engineering)*, **15**(11):896-913. http://dx.doi.org/10.1631/jzus.A1400117

Fahimifar, A., Karami, M., Fahimifar, A., 2015. Modifications to an elasto-visco-plastic constitutive model for prediction of creep deformation of rock samples. *Soils and Foundations*, **55**(6):1364-1371. http://dx.doi.org/10.1016/j.sandf.2015.10.003

Han, L.H., Yang, Y.F., 2007. Modern Steel Tube Confined Concrete Structures Technology. China Architecture & Building Press, Beijing, China, p.75-102 (in Chinese).

Hegde, A.M., Sitharam, T.G., 2015. Three-dimensional numerical analysis of geocell-reinforced soft clay beds by considering the actual geometry of geocell pockets. *Canadian Geotechnical Journal*, **52**(9):1396-1407. http://dx.doi.org/10.1139/cgj-2014-0387

Itasca Consulting Group Inc., 2005. Fast Lagrangian Analysis of Continua in 3 Dimensions, Version 3.0, User's Manual. Itasca Consulting Group, Inc.

Jiao, Y.Y., Song, L., Wang, X.Z., *et al*., 2013. Improvement of the U-shaped steel sets for supporting the roadways in loose thick coal seam. *International Journal of Rock Mechanics & Mining Sciences*, **60**:19-25. http://dx.doi.org/10.1016/j.ijrmms.2012.12.038

Latha, G.M., Garaga, A., 2012. Elasto-plastic analysis of jointed rocks using discrete continuum and equivalent continuum approaches. *International Journal of Rock Mechanics and Mining Sciences*, **53**:56-63. http://dx.doi.org/10.1016/j.ijrmms.2012.03.013

Li, S.C., Feng, X.D., Li, S.C., 2013. Numerical model for the zonal disintegration of the rock mass around deep underground workings. *Theoretical and Applied Fracture Mechanics*, **67-68**:65-73. http://dx.doi.org/10.1016/j.tafmec.2013.11.005

Li, T.C., Lyu, L.X., Zhang, S.L., *et al*., 2015. Development and application of a statistical constitutive model of damaged rock affected by the load-bearing capacity of damaged elements. *Journal of Zhejiang University-SCIENCE A (Applied Physics & Engineering)*, **16**(8):644-655. http://dx.doi.org/10.1631/jzus.A1500034

Li, W.T., Yang, N., Li, T.C., 2016. Implementation of bolt broken failure in FLAC^{3D} and its application. *Chinese Journal of Rock Mechanics and Engineering*, **35**(4):753-767 (in Chinese). http://dx.doi.org/10.13722/j.cnki.jrme.2015.0060

Liu, W., Alber, B., Zhao, Y., *et al*., 2016. Upper bound analysis for estimation of the influence of seepage on tunnel face stability in layered soils. *Journal of Zhejiang University-SCIENCE A (Applied Physics & Engineering)*, **17**(11):886-902. http://dx.doi.org/10.1631/jzus.A1500233

Nemcik, J., Ma, S., Aziz, N., *et al*., 2014. Numerical modelling of failure propagation in fully grouted rock bolts subjected to tensile load. *International Journal of Rock Mechanics and Mining Sciences*, **71**:293-300. http://dx.doi.org/10.1016/j.ijrmms.2014.07.007

Pourhosseini, O., Shabanimashcool, M., 2014. Development of an elasto-plastic constitutive model for intact rocks. *International Journal of Rock Mechanics and Mining Sciences*, **66**:1-12. http://dx.doi.org/10.1016/j.ijrmms.2013.11.010

Qi, T.Y., Lu, S.L., Gao, B., 2004. Amended model of bolt element in FLAC and its application. *Chinese Journal of Rock Mechanics and Engineering*, **23**(13):2197-2200 (in Chinese).

Rodríguez, R., Díaz-Aguado, M.B., 2013. Deduction and use of an analytical expression for the characteristic curve of a support based on yielding steel ribs. *Tunnelling and Underground Space Technology*, **33**:159-170. http://dx.doi.org/10.1016/j.tust.2012.07.006

SAC (Standardization Administration of China), 2014. Technical Code for Concrete Filled Steel Tubular Structures, GB 50936-2014. China Construction Industry Press, Beijing, China (in Chinese).

Schumacher, F.P., Kim, E., 2013. Modeling the pipe umbrella roof support system in a Western US underground coal mine. *International Journal of Rock Mechanics and Mining Sciences*, **60**:114-124. http://dx.doi.org/10.1016/j.ijrmms.2012.12.037

Wang, C., Wang, Y., Lu, S., 2000. Deformational behaviour of roadways in soft rocks in underground coal mines and principles for stability control. *International Journal of Rock Mechanics and Mining Sciences*, **37**(6):937-946. http://dx.doi.org/10.1016/S1365-1609(00)00026-5

Wang, Q., Jiang, B., Li, S.C., *et al*., 2016a. Experimental studies on the mechanical properties and deformation & failure mechanism of U-type confined concrete arch

centering. *Tunnelling and Underground Space Technology*, **51**:20-29.
http://dx.doi.org/10.1016/j.tust.2015.10.010

Wang, Q., Jiang, B., Shao, X., *et al*., 2016b. Mechanical properties of square-steel confined-concrete quantitative pressure-relief arch and its application in a deep mine. *International Journal of Mining, Reclamation and Environment*, **30**(5):438-460.
http://dx.doi.org/10.1080/17480930.2015.1105648

Wang, S.H., Qi, J.L., Yu, F., *et al*., 2016. A novel modeling of settlement of foundations in permafrost regions. *Geomechanics and Engineering*, **10**(2):225-245.
http://dx.doi.org/10.12989/gae.2016.10.2.225

Wong, L.N.Y., Fang, Q., Zhang, D., 2013. Mechanical analysis of circular tunnels supported by steel sets embedded in primary linings. *Tunnelling and Underground Space Technology*, **37**:80-88.
http://dx.doi.org/10.1016/j.tust.2013.03.011

Wu, H.M., Shu, Y.M., Zhu, J.G., 2011. Implementation and verification of interface constitutive model in FLAC^{3D}. *Water Science and Engineering*, **4**(3):305-316.
http://dx.doi.org/10.3882/j.issn.1674-2370.2011.03.007

You, C.A., 2000. Calculation Theory of Roadway Steel Support. China Coal Industry Publishing House, Beijing, China, p.45-67 (in Chinese).

Yu, Y., Bathurst, R.J., Damians, I.P., 2016a. Modified unit cell approach for modelling geosynthetic-reinforced column-supported embankments. *Geotextiles and Geomembranes*, **44**(3):332-343.
http://dx.doi.org/10.1016/j.geotexmem.2016.01.003

Yu, Y., Bathurst, R.J., Allen, T.M., 2016b. Numerical modeling of the SR-18 geogrid reinforced modular block retaining walls. *Journal of Geotechnical and Geoenvironmental Engineering*, **142**(5):04016003.
http://dx.doi.org/10.1061/(ASCE)gt.1943-5606.0001438

中文概要

题　目：基于 FLAC^{3D}梁单元修正的隧道/巷道拱架支护模拟方法

目　的：基于常用的数值模拟软件 FLAC^{3D}进行二次开发，弥补现有数值模拟方法的缺陷，提出一种准确有效的隧道/巷道拱架支护数值模拟方法。

创新点：1. 引入抗弯和抗压能力的相关性，改进梁单元压弯极限判据；2. 通过 FISH 语言编程，实现梁单元修正和拱架精确模拟。

方　法：1. 通过对 FLAC^{3D}中梁单元支撑理论的分析，明确其存在的缺陷，并利用算例进行证实（图 4~6）；2. 基于传统强度理论，对梁单元现有压弯极限判据进行改进（图 7 和 8）；3. 通过 FISH 语言编程，实现梁单元修正模型嵌入（图 9）；4. 通过算例分析，对新模拟方法的效果进行验证（图 10 和 13）。

结　论：1. 改进了梁单元压弯极限判据，通过 FISH 语言编程实现了梁单元的修正及拱架屈服失效的模拟。2. 构件压弯试验和巷道拱架支护实例分析表明：修正模型体现了在压弯组合荷载作用下梁单元屈服时弯矩和轴力的相关性；实现程序是有效的且灵敏度较高；提出的新模拟方法使计算偏差得到有效压制，拱架模型呈现出的力学行为及围岩支护作用更加接近实际，计算精度和设计可靠度更高。

关键词：隧道；拱架；FLAC^{3D}；梁单元；屈服判据；修正模型